Substitution Effect of Er^{3+} on Structural, Magnetic, and Optical Properties of Perovskite $BiFeO_3$

Pankaj Kumar[1] · Sourabh Sharma[2] · Sonia[1] · Harita Kumari[3] · Ashok Kumar[1] · Priya Saharan[4] · O. P. Thakur[2]

Abstract

This study aims to enhance the multiferroic properties of bismuth ferrite (BFO) by investigating the effects of substitution with erbium (Er) on the material's structural, optical, and magnetic characteristics. Er-substituted bismuth ferrite $(Bi_{1-x}Er_xFeO_3)$ ($x = 0$, 0.04, 0.08, 0.12, 0.16) nanoparticles (NPs) were synthesized via the very cost-effective Pechini modified sol–gel method followed by auto-combustion. X-ray diffraction (XRD) patterns confirmed the crystallinity, structure, and purity of the phase, revealing the formation of single-phase materials. The bond structure of the prepared samples was examined using Fourier transform infrared (FTIR) spectroscopy, confirming the significant stretching and bending of bonds of perovskites. Electron paramagnetic resonance (EPR) findings suggested a broadening of the signal as well as a shift of the center of resonance to lower fields. The experimental findings revealed that Er doping has a significant effect on the magnetic ordering and saturation magnetization of $BiFeO_3$. In addition, UV–Vis spectroscopy demonstrated that the energy bandgap in the prepared samples varies from 2.13 eV to 1.71 eV. This research contributes to an understanding of the enhanced structural, magnetic, and optical properties of Er-substituted BFO nanoparticles, which is useful for designing and developing multiferroic materials with enhanced magnetic functionality for next-generation magnetoelectric devices, optoelectronic devices, and photocatalysts.

Keywords Multiferroics · bismuth ferrite · spintronics · rare earth-doped BFO

Introduction

Multiferroic materials, which feature two or more ferroic properties (e.g., ferroelectric, ferromagnetic, ferroelastic) simultaneously in the same phase, and have become crucial, as they can be used in various advanced practical applications such as data storage devices, spintronics, magnetoelectric sensors, transducers, actuators, optoelectronic devices, and photocatalysts. The application of an electric, magnetic, or any stress field alters the ferroic properties and results in interesting practical applications.[1] There are numerous known multiferroic materials, including Cr_2O_3, $BiFeO_3$, $GaFeO_3$, and $BiMnO_3$. Among all these materials, bismuth ferrite (BFO) is a single-phase multiferroic material possessing both ferroelectric ($T_C = 830°C$) and G-type antiferromagnetic (AFM) ($T_N = 370°C$) properties at room temperature. BFO has an ABO_3 type perovskite structure along with a distorted rhombohedral unit cell with lattice parameters in the vicinity of $a = b = 5.58$ Å, $c = 13.90$ Å.[2–4] Various morphologies including sheets, cubes, flowers,

Pankaj Kumar and Sourabh Sharma have contributed equally to this work.

✉ Ashok Kumar
ashokkumar.phy@dcrustm.org

✉ O. P. Thakur
opthakur@nsut.ac.in

1 Nano Research Laboratory, Deenbandhu Chhotu Ram University of Science and Technology, Murthal, Haryana 131039, India

2 Materials Analysis and Research Laboratory, Netaji Subhas University of Technology, Dwarka, New Delhi 110078, India

3 Department of Physics, Maharshi Dayanand University, Rohtak, Haryana 124001, India

4 Centre of Excellence for Energy and Environmental Studies, Deenbandhu Chhotu Ram University of Science and Technology, Murthal, Sonipat, Haryana 131039, India

octahedrons, rods, wires, and groove-like shapes have been observed based on the synthesis method employed.[5] BFO belongs to the R-3c space group, and larger Bi^{3+} cations reside on the A site, while Fe^{3+} ions occupy the B site. The ferroelectricity in BFO arises because of the displacement of Fe^{3+} and Bi^{3+} ions with respect to the [111] direction of the unit cell, while antiferromagnetic behavior arises due to the partially filled d orbitals in Fe^{3+} ions. BFO and BFO-based materials hold promise for their application in sensing, data storage devices, and spintronics, among others.[6] Numerous investigations have concentrated on modifying ferromagnetic behavior or ferroelectric polarization through the application of external fields.

With all these notable properties, the synthesis of pristine BFO is a challenging task. During high-temperature synthesis, stable phases such as $Bi_{25}FeO_{40}$ and $Bi_2Fe_4O_9$ become viable, and the presence of these phases may cause an increase in the leakage current, which leads to poor conductivity and other properties such as low remanent polarization.[7] Therefore, to enhance the various properties of BFO, these stable impure phases should be suppressed, which can be done by means of substitution or doping. Substitution is the key to enhancing various properties of any material. Thus, these phases can be suppressed by substitution of other ions at A and B sites, which may enhance the ferroelectric and ferromagnetic properties of BFO. Substitution results in structural distortion, leading to reduced crystallite size and enhanced magnetoelectric coupling. As single-phase pristine BFO shows a G-type AFM nature with a magnetic spiral structure of about 62 nm, which cancels the ferromagnetic effect and bounds the magnetoelectric effect, the magnetic properties of partially substituted BFO nanoparticles are similarly enhanced as the spin cycloid structure collapses by means of structural transitions. A number of transition series and rare earth (RE) elements have been used as dopants for this purpose. It has been reported that doping with RE elements La, Sm, Y, Gd, and Er can suppress the impure/secondary phases in BFO.[8] For instance, the introduction of La doping initiates a transition in the structural configuration from rhombohedral to orthorhombic. Doping of RE elements not only changes the structure but also enhances the ferroelectric and ferromagnetic properties. These changes are generally observed when the particle size decreases to under 60 nm.[9] A significant number of research articles have reported on the enhancement of various properties of BFO by doping of RE (Sm, Nd, etc.) or transition elements (Co, Mn, etc.) at both A and B sites. Generally, it is observed that doping of RE elements at the A site results in the enhancement of magnetic properties, while doping of transition elements at the B site will enhance their ferroelectric properties.[10]

Acharaya et al. synthesized Er-doped nanocrystalline BFO using a chemical route, revealing the presence of $Bi_2Fe_4O_9$ (~2.4% relative to R-3c phase) with 10% Er.[11] They observed a sharp transition from AFM to FM state below the T_N and noted an increase in remanent magnetization of approximately 0.5 emu/g at room temperature. Guo et al. examined Er-doped $BiFeO_3$ nanoparticles ($0.05 < x < 0.25$), finding impurity phases for $x = 0.10$ and measuring the highest magnetization value of 1.5 emu/g at room temperature for this composition.[12] BFO, a multiferroic material at room temperature, presents an appealing option due to its visible light activity and magnetic behavior aiding in easy catalyst retrieval. Its narrow bandgap of 2.1–2.7 eV enhances its photocatalytic activity under visible light, crucial given that visible light accounts for about 48% of total solar energy.[13] There is further need to study the optical properties and enhanced magnetic properties of Er^{3+}-substituted BFO to explore the potential applications. For the fabrication of perovskite single-phase material, an array of soft-chemistry methodologies have been developed to synthesize $BiFeO_3$ (including hydrothermal and microwave/hydrothermal, sol–gel, sonochemical, co-precipitation, and molten salt methods). We have devised a quick $BiFeO_3$ synthesis method employing a sol–gel auto-combustion route, and synthesized $Bi_{1-x}Er_xFeO_3$ ($x = 0$, 0.04, 0.08, 0.12, 0.16) nanoparticles for studying various structural, optical, and magnetic properties.

Synthesis of Nanoparticles

Chemicals

$Bi(NO_3)_3 \cdot 5H_2O$ (Sisco Research Laboratories [SRL], purity > 98.5%), $Fe(NO_3)_3 \cdot 9H_2O$ (SRL, purity > 98%), $Er(NO_3)_3 \cdot 5H_2O$ (SRL, purity > 99.9%), anhydrous citric acid, and distilled water (DW) were used to prepare the samples.

Synthesis of $Bi_{1-x}Er_xFeO_3$ Nanoparticles

Er-doped bismuth ferrite ($Bi_{1-x}Er_xFeO_3$, $x = 0.04$, 0.08, 0.12, 0.16) NPs were prepared by Pechini's modified sol–gel auto-combustion route.[14] The precursors were dissolved individually in 20 ml of DW in separate beakers in proper stoichiometric ratios for 15 min on a magnetic stirrer. The homogeneous solutions were then mixed individually dropwise through a burette in a beaker with 50 ml distilled water with continuous stirring. A total of 8–9 g anhydrous citric acid ($C_6H_8O_7$) was used as a chelating agent and added to the solution. The liquid NH_3 (25%) was then added to achieve a neutral pH, after which the solution was maintained on a hot plate/magnetic stirrer at 80°C for 4–5 h until the solution became a viscous resin/gel. Following the gel formation, the hot plate temperature was increased to approximately 300°C

to initiate the auto-combustion process. Subsequently, a thick powder was produced and eventually pulverized using an agate mortar and pestle. The nanoparticles of Er-doped BFO were obtained after annealing them in a muffle furnace at 600°C for 6 h with a heating rate of 5°C/min. A schematic presentation of the synthesis route is illustrated in Fig 1.

Characterization Techniques

The structural parameters were calculated by an x-ray powder diffractometer (Malvern Panalytical, Empyrean) with CuK_α radiation ($\lambda = 1.54$ Å) functioning at 60 kV, and Fourier transform infrared (FTIR) spectroscopy was performed using a Thermo Scientific Nicolet iS50 spectrophotometer. The magnetic field strength–magnetization (M–H) loop was analyzed with a vibrating-sample magnetometer (VSM) (MicroSense ADE-EV9) for ±10 KOe field, and the electron paramagnetic resonance (EPR) study of the synthesized NPs was undertaken using a Bruker A300 instrument, which was operated at a microwave frequency of 9.6 GHz at room temperature. The energy bandgap was determined using a Shimadzu UV-3600i Plus UV-Vis-NIR spectrophotometer. All these findings are discussed in detail in the following section.

Results and Discussion

X-ray Diffraction (XRD) Analysis

The confirmation of the formation of phase identification and structural nanoparticles in their as-prepared state was carried out through XRD. Figure 2 illustrates the XRD patterns of pure and Er-substituted BFO NPs with varying Er
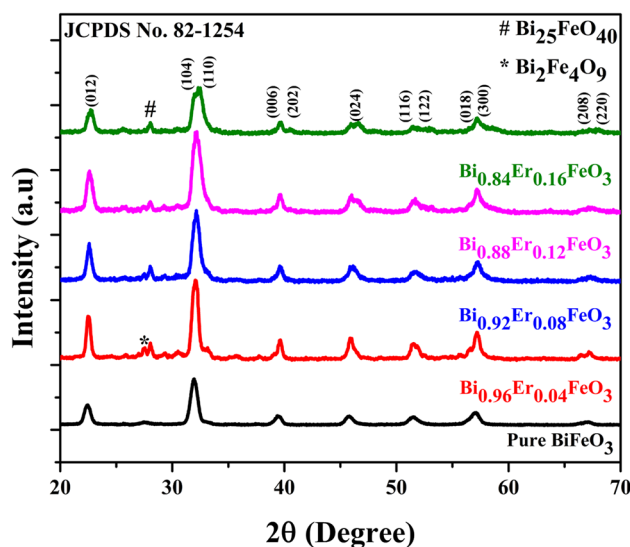
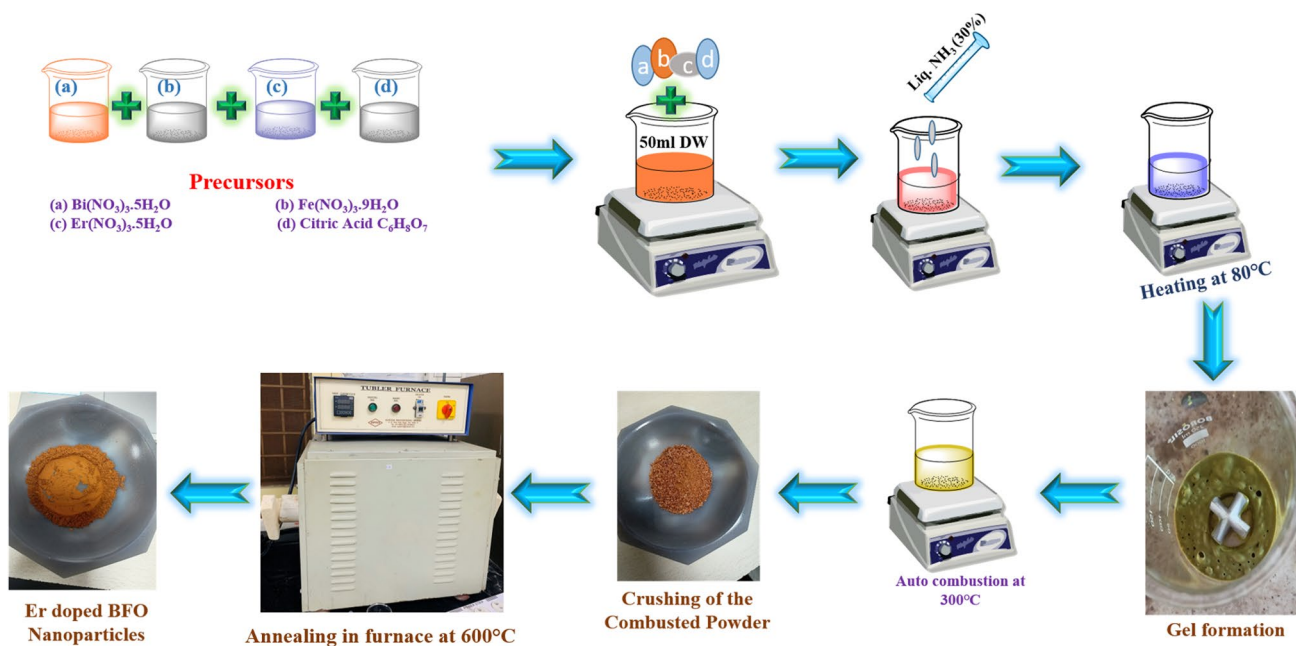**Fig. 2** XRD patterns of $Bi_{1-x}Er_xFeO_3$ ($x = 0$, 0.04, 0.08, 0.12, 0.16) nanoparticles.

Fig. 1 Schematic representation of synthesis route of $Bi_{1-x}Er_xFeO_3$ ($x = 0$, 0.04, 0.08, 0.12, 0.16) nanoparticles.

concentrations. XRD was conducted within an angular range of 20°–70°, and the indexed diffraction peaks of the samples indicate the existence of the rhombohedral phase as the primary phase, where the split peaks with (104) and (110) indexing are the defining peaks of the pristine BFO. The peaks at around 28° and 28.5° are attributed to the secondary phases of $Bi_2Fe_4O_9$ and $Bi_{25}FeO_{40}$, respectively, which may arise due to the volatile nature of bismuth at high temperatures. These phases do not affect the multiferroic properties of the prepared samples, as these secondary phases do not alter the ferroelectric properties at room temperature.[15,16] The calculated values are shown in Table I. All XRD patterns obtained correspond to a rhombohedral phase (JCPDS file no. 82-1254) with an R-3c space group. It is apparent that the dopant does not affect the structural integrity of BFO. However, doping does result in a minor impurity peak around 28°. Comparison with JCPDS data shows that this impurity peak corresponds to $Bi_2Fe_4O_9$ (mullite).[17]

The Debye–Scherrer equation and Bragg's equation were used to calculate the crystallite sizes, interplanar spacing, and lattice parameters. The crystallite sizes of the synthesized NPs were determined with the Debye–Scherrer equation

$$D = \frac{k\lambda}{\beta \cos \theta},$$

where k is the shape factor, β is the full width at half maximum (FWHM) in radians, λ is the wavelength of the x-rays (CuK$_\alpha$ $\lambda = 1.54$ Å), and θ is the Bragg angle. The interplanar spacing was calculated using Bragg's equation

$$2d_{hkl}\mathrm{Sin}\theta_{hkl} = n\lambda,$$

and dislocation density was calculated using the following equation:

$$\delta = \frac{1}{D^2}.$$

Clearly, the Er substitution did not alter the crystallographic symmetry. The dislocation density quantifies crystallinity, and an increase in its value predicts a decrease in the crystallite size of NPs. The dislocation density values were calculated using the crystallite sizes computed by the Scherrer method.[18] With an increase in the concentration

of Er, the dislocation density increases because of the ionic radii size difference of the Er^{3+} and Bi^{3+} ions, resulting in the deformation of the structure from rhombohedral to distorted rhombohedral. $Bi_{0.96}Er_{0.04}FeO_3$ has the largest crystallite size (12.7 nm), while the $Bi_{0.84}Er_{0.16}FeO_3$ sample has the smallest crystallite size of 7.9 nm. It was found that with an increase in the concentration of Er^{3+} ions, the average crystallite size of the nanoparticles decreases.

Fourier Transform Infrared (FTIR) Spectroscopy

Figure 3 shows FTIR graphs of the prepared samples. The variation in the peak position, shape, and width of FTIR spectra is due to the variation in the local defects and grain size of the NPs. The peak positions in the FTIR graph at 430 cm^{-1} and 530 cm^{-1} are related to Fe–O stretching and Fe–O bending vibrations, respectively.[19,20] This behavior is typical of FeO$_6$ octahedra that are found in perovskites. The peak near 1633 cm^{-1} relates to the symmetric stretching of H$_2$O. The peak around 1393 cm^{-1} is due to nitrate trapped in the sample, which could be the residual of nitrate precursors.[21] Peaks at 847 cm^{-1} correspond to Bi–O bond vibrations. Notably, while the tetrahedral group peak at 430 cm^{-1} remains stable, the octahedral group shifts from 530 to 515 cm^{-1}, indicating Fe–O vibrational mode
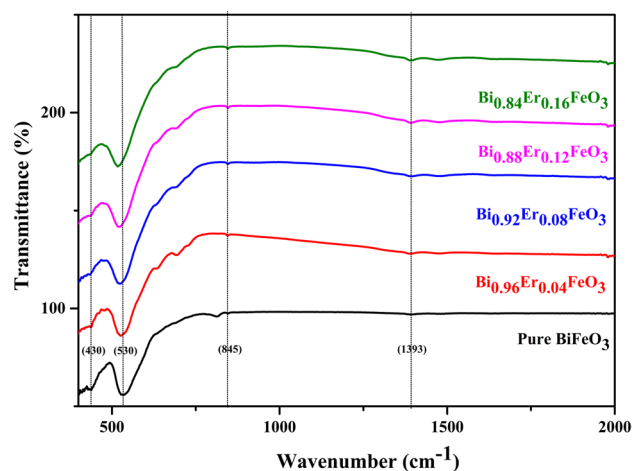

Fig. 3 FTIR graph of $Bi_{1-x}Er_xFeO_3$ ($x = 0$, 0.04, 0.08, 0.12, 0.16) nanoparticles.

Table I Lattice parameters, crystallite size, interplanar spacing, and dislocation density of synthesized nanoparticles calculated using XRD patterns

Sample	$a = b$ (Å)	c (Å)	D (nm)	d_{hkl} (nm)	$\delta \times 10^{-4}$ (nm^{-2})
$BiFeO_3$	5.545	13.79	11.2	2.79	79.71
$Bi_{0.96}Er_{0.04}FeO_3$	5.538	13.71	12.7	2.78	62.00
$Bi_{0.92}Er_{0.08}FeO_3$	5.549	13.82	10.4	2.78	92.45
$Bi_{0.88}Er_{0.12}FeO_3$	5.561	13.87	8.9	2.77	12.62
$Bi_{0.84}Er_{0.16}FeO_3$	5.568	13.89	7.9	2.76	16.02

compression.[22] A gradual shift of the absorption peak of Fe–O stretching vibration with the increase in Er substitution percentage towards a lower wave number shows that various Er substituents have been absorbed into the lattice site of bismuth ferrite. This also indicates the occurrence of a structural transition with respect to different substitution percentages of Er^{3+} ions. Er substitution leads to the change in structural environments and the bonding within the lattice, which results in the FTIR peaks with respect to pure BFO.

Vibrating-Sample Magnetometry (VSM)

The M–H loop of the prepared samples is shown in Fig. 4a, and the trend of remanent magnetization and enlarged image of the M–H curve is shown in Fig. 4b to elucidate the small ferromagnetic nature of the samples. The trend of saturation magnetization of each sample with an increasing concentration of Er doping is evident in Fig. 4b and c. The calculated values from the M–H loop are shown in Table II.

Observations indicate that the mild ferromagnetic behavior of bismuth ferrite, possessing a perovskite structure, is significantly influenced by the rotation of FeO_6 octahedra in relation to each other.[23] The value of saturation magnetization, M_s (in emu/g), varies from 4.259 to 1.156 while the value of remanent magnetization, M_r (in emu/g), varies from 1.268 to 0.227 with increasing Er^{3+} concentration. The values of M_s and M_r decrease rapidly with Er^{3+} concentration because smaller particles are easier to demagnetize, and coercivity (H_c) declines with increasing Er^{3+} concentration. BFO comprises a G-type AFM ordering along the $[001]_{hex}$ axis in its hexagonal representation, which is anticipated to result in minimal spontaneous magnetization.[24,25] The Dzyaloshinskii–Moriya interaction partially breaks antiferromagnetic ordering, causing a tiny magnetic moment. Due to electron exchange coupling, samples with small crystallites become superparamagnetic.[26] The reduced size of these particles makes them superparamagnetic for $x = 0.04$–0.16. Superparamagnetic particles have low coercivity/retentivity and significant magnetism. The interaction between erbium's 4f electrons and iron's 3d electrons leads to a partial disruption of the antiferromagnetic coupling between the Fe^{3+} ions.[27] The enormous quantity of uncompensated Fe^{3+} ion spins at the particle surface breaks the spin cycloidal structure, which is the reason for the significant magnetization in the prepared samples.[28]

Electron Paramagnetic Resonance (EPR) Analysis

EPR is an extremely efficient spectroscopic technique utilized to evaluate the magnetic properties of nanoparticles which involves the examination of diverse magnetic factors such as spin–spin relaxation, magnetic anisotropy, super-exchange interactions, and dipolar interactions.

Table II Magnetic parameters calculated from M–H curves, including saturation magnetization, remanent magnetization, coercivity, and squareness ratio of synthesized nanoparticles

Sample	M_s emu/g	M_r emu/g	H_c Oe	Squareness ratio
$BiFeO_3$	4.259	1.268	222.73	0.2977
$Bi_{0.96}Er_{0.04}FeO_3$	3.158	0.729	179.03	0.2308
$Bi_{0.92}Er_{0.08}FeO_3$	2.547	0.414	137.80	0.1625
$Bi_{0.88}Er_{0.12}FeO_3$	1.877	0.424	192.86	0.2258
$Bi_{0.84}Er_{0.16}FeO_3$	1.156	0.227	177.47	0.1963

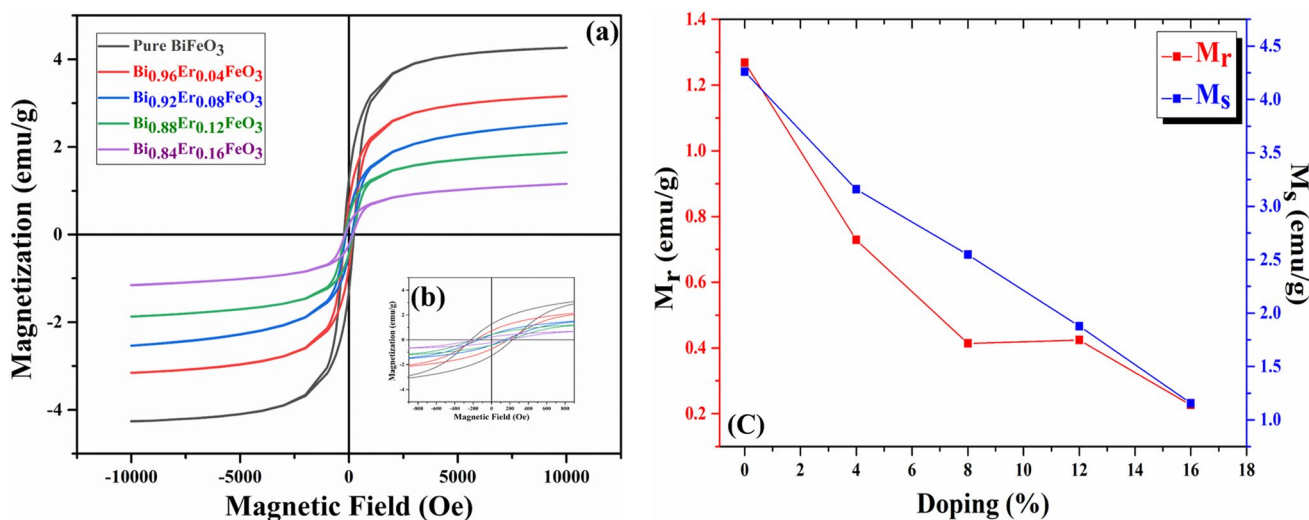**Fig. 4** (a) M–H loops of $Bi_{1-x}Er_xFeO_3$ ($x = 0$, 0.04, 0.08, 0.12, 0.16) nanoparticles. (b) Enlarged image of M–H loop to demonstrate the ferromagnetic character of the samples. (c) Variation in M_r and M_s with Er substitution.

Table III EPR parameters g_{eff}, resonance field, sweep width, and center of resonance calculated from EPR spectra of synthesized nanoparticles

Sample	g_{eff}	H_r(G)	ΔH_{PP} (G)	$\Delta H_{1/2}$ (G)
$BiFeO_3$	2.583	2670.11	1932.48	3347.15
$Bi_{0.96}Er_{0.04}FeO_3$	2.549	2705.92	1834.63	3177.67
$Bi_{0.92}Er_{0.08}FeO_3$	2.453	2811.91	1696.86	2939.04
$Bi_{0.88}Er_{0.12}FeO_3$	2.438	2828.64	1784.58	3090.98
$Bi_{0.84}Er_{0.16}FeO_3$	2.387	2888.88	1783.26	3088.69

These parameters can be determined by analyzing the g-factor, resonance field, and sweep width. The various parameters, as shown in Table III, were calculated using Eqs. 1 and 2.[29]

$$g = \frac{h\upsilon}{\mu_B H_r}, \tag{1}$$

$$\Delta H_{1/2} = \sqrt{3}\Delta H_{PP}. \tag{2}$$

where h represents Planck's constant, H_r denotes the resonant magnetic field, and μ_B symbolizes the Bohr magneton ($\mu_B = 6.27 x 10^{-24} J/T$), with υ indicating the frequency of electromagnetic radiation.

Er ions interacting with the BFO lattice alter the local magnetic environment, impacting EPR spectra. Interactions between neighboring Er ions, like dipole–dipole or exchange interactions, influence magnetic behavior, affecting parameters such as line width and saturation magnetization. Magnetic clusters, formed by Er ion aggregation or structural defects lead to complex interactions, causing deviations in EPR spectra, emphasizing the importance of local magnetic environments in Er-doped BFO. As depicted in Fig. 5, as x increases from 0.04 to 0.12, the center of resonance field ($H_{1/2}$) of EPR signals transitions toward a lower magnetic field, from 3347 G to 3088 G. The existence of a nonhomogeneous local magnetic field is responsible for both the observed broadening of the signal as well as a shift of the center of resonance to lower fields. This is due to the presence of a nonhomogeneous local magnetic field that modifies the signal's resonance field and line shape.[30–32] In addition, a decrease in their sweep width from $\Delta H_{pp} = 1932$ to 1783 G was observed as x increased from 0.04 to 0.12. The results of EPR resemble the results of VSM; the sweep width decreases, and the peak becomes intense as saturation magnetization decreases.

The squareness ratio of Er-doped bismuth ferrite (BFO) EPR spectra reveals magnetic properties. We observed a consistent decrease in the squareness ratio with higher Er
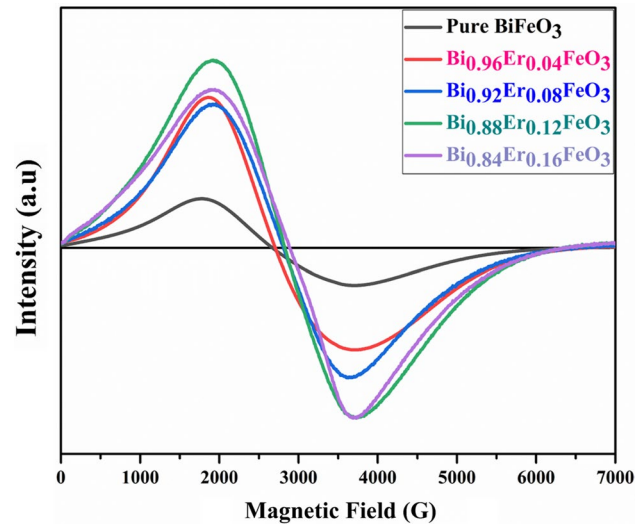
Fig. 5 EPR spectra of $Bi_{1-x}Er_xFeO_3$ (x = 0, 0.04, 0.08, 0.12, 0.16) nanoparticles.

ion concentration, indicating disrupted magnetic interactions. An anomaly at 12% Er doping suggests unique magnetic interactions or structural changes, possibly due to magnetic cluster formation.

UV–Vis Spectroscopy

UV–Vis spectroscopy of the synthesized nanoparticles provides information about bandgap energy, which varies from 2.13 eV to 1.71 eV, as shown in Fig. 6. For pristine BFO, the O 2p state of BFO generally hybridized with that of the Fe 3d state, which forms bonding and antibonding orbitals. The bonding orbital formed is the valence band generally known as the O 2p band, while the antibonding orbital or Fe 3d band is the conduction band. Transition between these formed valence and conduction bands determines the energy bandgap.[33,34] Thus, to examine the bandgap of the prepared samples, UV–Vis spectroscopy was performed in the wavelength range of 200–800 nm. The energy bandgap (E_g) was determined using the Kubelka–Munk function[35] with the following equations:

$$\alpha h\upsilon = A(h\upsilon - E_g)^n,$$

$$\alpha = \frac{(1-R)^2}{2R},$$

where n is 1/2 for direct transitions, R is diffused reflectance, h is the Planck constant, υ is light frequency, A is an energy-dependent constant, and α is the absorption coefficient. Figure 6 presents the Tauc plot of the synthesized nanoparticles,
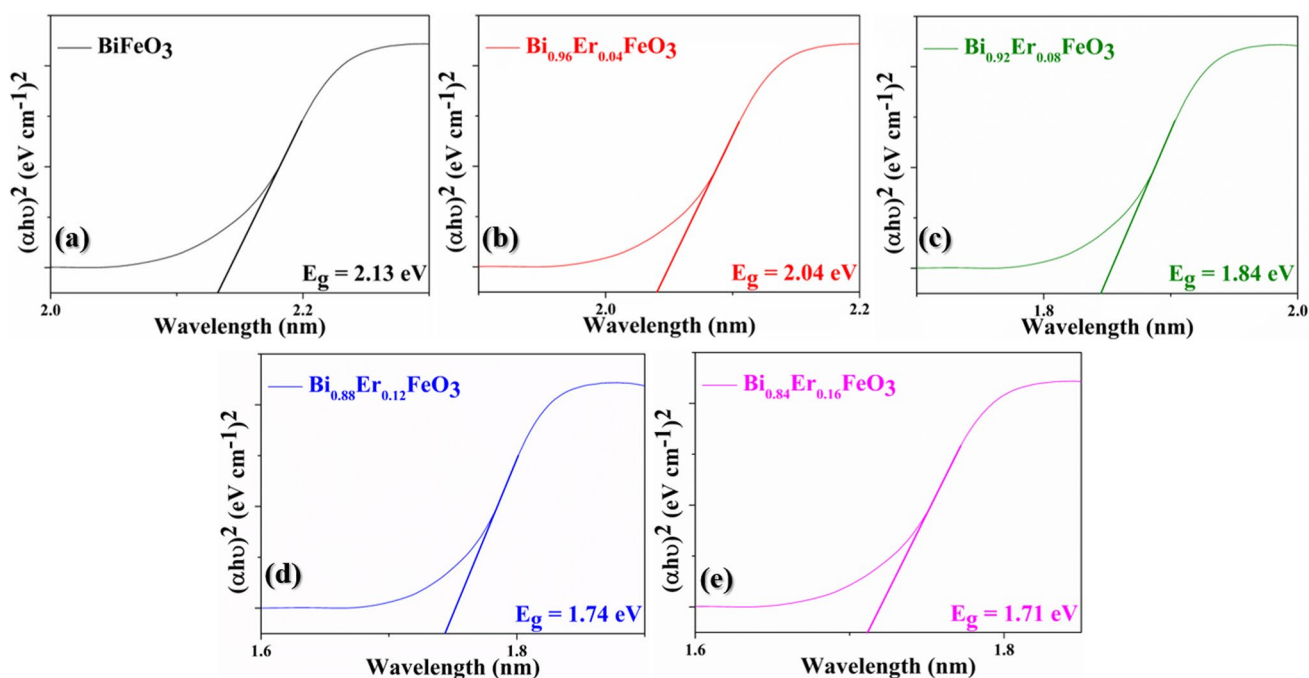
Fig. 6 Tauc's plot of synthesized nanoparticles.

Table IV Calculated energy bandgap of synthesized nanoparticles

Composition	Energy bandgap, E_g (eV)
$BiFeO_3$	2.13
$Bi_{0.96}Er_{0.04}FeO_3$	2.04
$Bi_{0.92}Er_{0.08}FeO_3$	1.84
$Bi_{0.88}Er_{0.12}FeO_3$	1.74
$Bi_{0.84}Er_{0.16}FeO_3$	1.71

and the E_g values calculated using Tauc's plot are presented in Table IV.

The decrease in the bandgap (E_g) value with higher substitution percentage is ascribed to structural distortion and reduced hybridization, which may reduce the effective bandgap related to Er's electronic configuration. Additionally, the decrease in crystallite size as the substitution percentage increases could contribute to this trend. Conversely, a slight increase in the bandgap value for $Bi_{0.84}Er_{0.16}FeO_3$ may be attributed to surface and interface effects. The lower bandgap energy observed in the synthesized nanoparticles renders them suitable for photocatalytic applications in the visible region.[36,37]

Conclusion

$Bi_{1-x}Er_xFeO_3$ ($x = 0$, 0.04, 0.08, 0.12, 0.16) NPs were prepared via Pechini's modified sol–gel method followed by auto-combustion. The structure of the prepared samples was analyzed by XRD, which confirmed the crystallinity of the powdered samples and the single-phase distorted rhombohedral structures with an R-3c space group. The characteristic bond vibrations and stretching were confirmed with FTIR analysis for the characteristic behavior of FeO_6 octahedra in perovskites. Magnetic studies were performed by plotting M–H loops and EPR spectra, and a decrease in M_r, M_s, and H_c values was observed with an increase in the Er^{3+} concentration in the prepared nanoparticles, which was due to the superparamagnetic behavior of the NPs with an increase in the doping concentration. With a reduction in saturation magnetization, the sweep width narrowed and the EPR signal intensity increased. The results of VSM and EPR data are in accord with each other. With these findings, the AFM nature of these materials makes them suitable for application in magnetoelectric (ME) devices, and as the spin interaction plays a major role, these materials can be used in spintronics. Further studies of the NPs can investigate their ferroelectric properties, photocatalytic properties, and enhanced adsorption (α_{ME}) so that the scope of applications such as gas sensing, data storage, and environmental applications like dye degradation and heavy metal sensing can be explored.

Author contributions Pankaj Kumar: conceptualization, methodology, formal analysis, investigation, writing—original draft. Sourabh Sharma: conceptualization, methodology, formal analysis, investigation, writing—original draft. Sonia and Harita Kumari: formal analysis, writing—review and editing. Ashok Kumar, Priya Saharan, and O. P. Thakur: conceptualization, supervision, resources, methodology, roles, and writing—review and editing.

Conflict of interest The authors declare that they are not aware of any personal or financial conflicts that might have appeared to affect the research reported in this study. The research submitted is carried out in compliance with relevant institutional biosafety and biosecurity protocols.

References

1. T.D. Rao, T. Karthik, and S. Asthana, Investigation of structural, magnetic and optical properties of rare earth substituted bismuth ferrite. *J. Rare Eart.* 31, 370 (2013).
2. G. Catalan and J.F. Scott, Physics and applications of bismuth ferrite. *Adv. mater.* 21, 2463 (2009).
3. T. Sahu and B. Behera, Dielectric, electrical and magnetic study of rare-earth-doped bismuth ferrite lead titanate. *App. Phys. A* 125, 1 (2019).
4. V. Verma, Structural, electrical and magnetic properties of rare-earth and transition element co-doped bismuth ferrites. *J. Alloys Compd.* 641, 205 (2015).
5. F. Shahrab and A. Tadjarodi, Exploring the role of fuel in the synthesis of bismuth ferrite nanoparticles by microwave-assisted combustion in solid state and the study of photocatalytic degradation of Brilliant Blue. *J. Mol. Struct.* 1295, 136806 (2024).
6. S. Godara, N. Sinha, G. Ray, and B. Kumar, Combined structural, electrical, magnetic and optical characterization of bismuth ferrite nanoparticles synthesized by auto-combustion route. *J. Asian Ceram. Soc.* 2, 416 (2014).
7. S.E. Ali, A.M. Abdelghany, and Y.M. Abbas, Structural and magnetic quantification of rhombohedral–orthorhombic phase transition in gadolinium substituted bismuth ferrite. *J. Magn. Magn. Mater.* 572, 170600 (2023).
8. P.C. Sati, M. Arora, S. Chauhan, M. Kumar, and S. Chhoker, Effect of Dy substitution on structural, magnetic and optical properties of $BiFeO_3$ ceramics. *J. Phys. Chem. Solids* 75, 105 (2014).
9. Z.X. Cheng, A.H. Li, X.L. Wang, S.X. Dou, K. Ozawa, H. Kimura, S.J. Zhang, and T.R. Shrout, Structure, ferroelectric properties, and magnetic properties of the La-doped bismuth ferrite. *J. Appl. Phys.* 103, 07E507 (2008).
10. S.G. Nair, J. Satapathy, and N.P. Kumar, Influence of synthesis, dopants, and structure on electrical properties of bismuth ferrite ($BiFeO_3$). *Appl. Phys. A* 126, 836 (2020).
11. S. Acharya, S. Sutradhar, J. Mandal, K. Mukhopadhyay, A.K. Deb, and P.K. Chakrabarti, Sol–gel derived nanocrystalline multiferroic $BiFeO_3$ and R^{3+} (R=Er and Tm) doped therein: magnetic phase transitions and enhancement of magnetic properties. *J. Magn. Magn. Mater.* 324, 4209 (2012).
12. J. Zhao, S. Liu, W. Zhang, Z. Liu, and Z. Liu, Structural and magnetic properties of Er-doped $BiFeO_3$ nanoparticles. *J. Nanopart. Res.* 15, 1969 (2013).
13. Y. Nassereddine, M. Benyoussef, B. Asbani, M.E. Marssi, and M. Jouiad, Recent advances toward enhanced photocatalytic proprieties of $BiFeO_3$-based materials. *Nanomaterials* 14, 51 (2023).
14. N. Sheoran, A. Kumar, V. Kumar, and A. Banerjee, Structural, optical, and multiferroic properties of yttrium (Y^{3+})-substituted $BiFeO_3$ nanostructures. *J. Supercond. Nov. Magn.* 33, 201 (2020).
15. K.S. Kumar, S. Ramu, A. Sudharani, M. Ramanadha, G. Murali, and R.P. Vijayalakshmi, Enhanced magnetic and dielectric properties of Gd doped $BiFeO_3$: Er nanoparticles synthesized by sol–gel technique. *Phys. E Low Dimens. Syst. Nanostruct.* 115, 113689 (2020).
16. A.K. Sahu, P. Mallick, S.K. Satpathy, and B. Behera, Effect on structural, electrical and temperature sensing behavior of neodymium doped bismuth ferrite. *Adv. Mater. Lett.* 12, 1 (2021).
17. S. Divya Lakshmi, I.B. Shameem Banu, R. Rajesh, M. Hafiz Mamat, and G. Gowri, Molecular design of $BiFeO_3$ via novel substitution by zirconium and erbium for tuning the multifunctional properties and band structure calculations. *Appl. Phys. A* 129, 552 (2023).
18. P. Jain, S. Shankar, and O.P. Thakur, Unveiling the impact of Ni^{2+}/Y^{3+} co-substitution on the structural, dielectric, and impedance properties of multiferroic spinel ferrite for hydroelectric cell application. *Phys. Chem. Chem. Phys.* 25, 21280 (2023).
19. N. Sheoran, M. Saini, A. Kumar, V. Kumar, T. Kumar, and M. Sheoran, Size dependent morphology, magnetic and dielectric properties of $BiFeO_3$ nanoparticles. *MRS Adv.* 4, 1659 (2019).
20. A. Wrzesińska, A. Khort, M. Witkowski, J. Szczytko, J. Ryl, J. Gurgul, D.S. Kharitonov, K. Łątka, T. Szumiata, and A. Wypych-Puszkarz, Structural, electrical, and magnetic study of La-, Eu-, and Er-doped bismuth ferrite nanomaterials obtained by solution combustion synthesis. *Sci. Rep.* 11, 22746 (2021).
21. Z. Nazeer, I. Bibi, F. Majid, S. Kamal, M.I. Arshad, A. Ghafoor, N. Alwadai, A. Ali, A. Nazir, and M. Iqbal, Optical, photocatalytic, electrochemical, magnetic, dielectric, and ferroelectric properties of Cd-and Er-doped $BiFeO_3$ prepared via a facile microemulsion route. *ACS Omega* 8, 24980 (2023).
22. K. Sarkar, H. Harsh, Z. Rahman, and V. Kumar, Enhancing the structural, optical, magnetic and ferroelectric properties of perovskite $BiFeO_3$ through metal substitution. *Chem. Phys. Impact* 8, 100478 (2024).
23. M. Zhang, V. Koval, Y. Shi, Y. Yue, C. Jia, J. Wu, G. Viola, and H. Yan, Magnetoelectric coupling at microwave frequencies observed in bismuth ferrite-based multiferroics at room temperature. *J. Mater. Sci. Tech.* 137, 100 (2023).
24. P.R. Vanga, P. Reddy, and M. Ashok, The effect of lanthanides (Er, Gd and La) on the adsorption and photocatalytic performance of bismuth ferrite. *MRS Adv.* 8, 849 (2023).
25. P. Suresh and S. Srinath, Study of, structure and magnetic properties of rare earth doped $BiFeO_3$. *Phys. B Condens. Matter.* 448, 281 (2014).
26. A. Pakalniškis, D. Zákutná, M. Gerina, G. Niaura, A. Zhaludkevich, D. Karpinsky, A. Normirzaev, R. Skaudžius, and A. Kareiva, Rhenium substitution effects on the structural, morphological and magnetic properties of bismuth ferrite $BiFe_{(1-x)}Re_xO_3$. *Ceram. Int.* 50, 10171 (2023).
27. S.D. Lakshmi, I.B. Shameem Banu, and R. Rajesh, Oxygen octahedra distortion-induced multiferroic properties of Er and Zr co-doped $BiFeO_3$ nanoparticles. *Int. J. Appl. Ceram. Tech.* 20, 1939 (2023).
28. S.D. Lakshmi, I.B. Shameem Banu, R. Rajesh, M. Hafiz Mamat, and G.V. Vijayaraghavan, Tuning the multiferroism and

magnetoelectric coupling of bismuth ferrite via substitutional defects by Er and transition metals (Nb/Zr/Y). *J. Supercond. Nov. Magn.Supercond. Nov. Magn.* 36, 1693 (2023).

29. G.S. Shahane, A. Kumar, M. Arora, R.P. Pant, and K. Lal, Synthesis and characterization of Ni–Zn ferrite nanoparticles. *J. Magn. Magn. Mater.* 322, 1015 (2010).

30. F. Yan, G. Xing, R. Wang, and L. Li, Tailoring surface phase transition and magnetic behaviors in $BiFeO_3$ via doping engineering. *Sci. Rep.* 5, 1 (2015).

31. Z. Ge, J. Zhu, H. Xue, and W. Mao, Structural phase transition and multiferric properties of Y Eu co-doped $BiFe097Mn003O3$ nanoparticles. *J. Mater. Sci. Mater. Electron.* 35, 36 (2024).

32. A.N. Ganie, M.U.D. Rather, and B. Want, Elucidating the structure, ferroic properties and magnetoelectric coupling in Dy-doped $BiFeO_3$ nanostructures. *J. Mater. Sci. Mater. Electron.* 35, 168 (2024).

33. A. Wrzesinska, A. Khort, I. Bobowska, A. Busiakiewicz, and A. Wypych-Puszkarz, Influence of the La^{3+}, Eu^{3+}, and Er^{3+} doping on structural, optical, and electrical properties of $BiFeO_3$ nanoparticles synthesized by microwave-assisted solution combustion method. *J. Nanomater.* 2019, 5394325 (2019).

34. S. Sharma, J.M. Siqueiros, and O.R. Herrera, Structural, dielectric, ferroelectric and optical properties of Er doped $BiFeO_3$ nanoparticles. *J. Alloys Compd.* 853, 156979 (2021).

35. C. Anthonyraj, M. Muneeswaran, S. Gokul Raj, N.V. Giridharan, V. Sivakumar, and G. Senguttuvan, Effect of samarium doping on the structural, optical and magnetic properties of sol–gel processed $BiFeO_3$ thin films. *J. Mater. Sci. Mater. Electron.* 26, 49 (2015).

36. C. Wu, J. Wei, and F. Kong, Effect of rare earth dopants on the morphologies and photocatalytic activities of $BiFeO_3$ microcrystallites. *J. Mater. Sci. Mater. Electron.* 24, 1530 (2013).

37. K.S. Kumar, M. Ramanadha, A. Sudharani, S. Ramu, and R.P. Vijayalakshmi, Structural, magnetic, and photoluminescence properties of $BiFeO_3$: Er-doped nanoparticles prepared by sol–gel technique. *J. Supercond. Nov. Magn.Supercond. Nov. Magn.* 32, 1035 (2019).